Hindawi
Advances in Materials Science and Engineering
Volume 2021, Article ID 9918834, 9 pages
https://doi.org/10.1155/2021/9918834

Research Article

Effect of CaO on the Autogenous Shrinkage of Alkali-Activated Slag Mortar

Dengdeng Zheng,[1] **Tao Ji**,[2] **and Guojie Wang**[1]

[1]*School of Engineering, Fujian Jiangxia University, Fuzhou, Fujian 350108, China*
[2]*College of Civil Engineering, Fuzhou University, Fuzhou, Fujian 350116, China*

Correspondence should be addressed to Tao Ji; jt72@fzu.edu.cn

Received 10 March 2021; Accepted 8 November 2021; Published 28 November 2021

Academic Editor: Guang Xing Liang

The autogenous shrinkage of alkali-activated slag (AAS) is significantly higher than that of ordinary Portland cement (OPC). The higher risk of concrete cracking due to autogenous shrinkage is a critical drawback to wider use of this promising alternative binder. The effect of CaO content on the autogenous shrinkage of AAS mortar was investigated. The autogenous shrinkage of AAS mortars was determined by comparator. The pore structure of the pastes was determined by mercury intrusion porosimetry. The hydration products of the pastes were determined by Fourier transform-infrared, thermogravimetric analysis, X-ray diffraction, and ^{29}Si solid-state magic-angle spinning nuclear magnetic resonance. The results show that the amount of portlandite increases as CaO content increases. CaO in the paste causes the partial replacement of C-S-H(I) (low stiffness) by C-S-H(II) (high stiffness). The hydration reaction of AAS is inhibited by the addition of CaO. The increase of polymerization degree of C-(A-)S-H and rearrangement of C-S-H(I) during hydration are inhibited by the addition of CaO, and micropores closure is also inhibited. Therefore, the autogenous shrinkage of AAS mortar decreases with the increase of CaO content.

1. Introduction

Ground granulated blast furnace slag (GGBFS) is a by-product of iron smelting. Alkali-activated GGBFS is a replacement for Portland cement in concrete. Alkali-activated slag (AAS) concrete has low embodied energy, a low CO_2 footprint, and equivalent or better strengths than ordinary Portland cement (OPC) concrete. AAS is also more resistant to fire, chloride-induced corrosion, and chemical (e.g., acid and sulfate) reactions than OPC [1]. However, a significant problem in using AAS is its volumetric instability. AAS concretes are prone to significant shrinkage due to self-desiccation and have a high risk of cracking [2]. There have been various studies over the past decade aimed at determining the influence of formula on autogenous shrinkage of AAS base material.

Allahverdi et al. [3] studied the effect of conditioning AAS mortar with liquid sodium silicate (LSS) on autogenous shrinkage. Autogenous shrinkage increased as the quantity of LSS increased. They concluded that the quantity of the activator greatly influenced the mechanical properties of the mortar, its porosity, and the degree of hydration, which are factors that determine autogenous shrinkage. Neto et al. [4] also studied the effect of adding LSS on the autogenous shrinkage of AAS mortar and reached the same conclusion.

Cartwright et al. [2] studied the effects of conditioning AAS mortar with NaOH and varying the LSS modulus on autogenous shrinkage. Autogenous shrinkage increased as quantities of NaOH increased and as the LSS modulus increased. They suggested that greater saturation, finer pore structure, lower elastic stiffness, and greater chemical shrinkage led to greater autogenous shrinkage. They also suggested that other mechanisms, such as creep and Gibbs–Bangham shrinkage, further contribute to greater autogenous shrinkage of AAS mortar and must be considered in future research.

Lee et al. [5] studied the effects of the proportion of slag, the quantity of sodium silicate powder, and the water/binder

ratio on the autogenous shrinkage of alkali-activated fly ash-slag (AFS) mortar. Autogenous shrinkage increased as the slag or sodium silicate content increased. For the same Na_2O/H_2O and SiO_2/H_2O ratios of alkali activators, the autogenous shrinkage of the AFS mortar increased as the water/binder ratio decreased. They attributed the greater autogenous shrinkage to greater capillary stress resulting from higher mesopore volume.

Neto et al. [6], Allahverdi et al. [3], and Lee et al. [5] all attributed the larger autogenous shrinkage of AAS or AFS mortar to its finer structure. Cartwright et al. [2] also suggested that creep is a factor in increased autogenous shrinkage of AAS mortar.

CaO can alter the initial Ca/Si ratio of AAS, which may lead to the change of the species and proportions of hydration products and modification of the structure of C-(A-)S-H. The expansion of CaO can also counter the autogenous shrinkage. To our knowledge, the effect of CaO on the autogenous shrinkage of AAS mortar, which was activated by NaOH, has not been reported. In this study, we investigated the effect of CaO (at proportions of 3%, 6%, 9%, and 12%) on the autogenous shrinkage of AAS mortar, using NaOH ($Na_2O\% = 4\%$ by mass of slag) as an activator.

2. Materials and Methods

2.1. Materials. GGBFS properties are given in Table 1, and its main chemical composition is shown in Table 2. NaOH powder was used as an alkaline activator. River sand was used as a fine aggregate. Properties of the fine aggregate are given in Table 3, and gradation of the fine aggregate (residue on each sieve) is given in Table 4.

2.2. Mixture Proportions. The compositions of AAS cement are provided in Table 5 and are denoted with specific codes. The labels m_{Na}, m_{Ca}, and m_s denote the NaOH content (by mass of Na_2O), the mass of CaO, and the mass of slag. The numbers 0, 3, 6, 9, and 12 denote the CaO content (% mass). The water/binder (GGBFS + activator) mass ratios of AAS mortars and pastes were 0.4. The sand/binder mass ratio of AAS mortars was 2 : 1.

2.3. Testing Methods. Three mortar cuboids measuring $25 \times 25 \times 280$ mm were cast for each group. Autogenous shrinkage tests were performed at ages 1, 2, 3, 4, 5, 6, 7, 9, 11, 14, 17, 21, 28, 35, 42, 49, 56, 63, 70, 77, 84, 91, 98, 112, 125, 140, 154, 168, 182, 196, 210, 224, 238, and 252 days. Length variances were determined in accordance with ASTM C490 [7]. All cuboids were wrapped with an inner layer of polyethylene film and an outer layer of aluminum foil and sealed with aluminum tape. The cuboids used for the autogenous shrinkage tests were demoulded at 24 h and immediately stored in a curing room at a constant temperature of $20 \pm 0.3^{\circ}$C. The paste specimens for the microscopic tests were prepared and cured using the same method.

The pore structure of the AAS pastes was measured using mercury intrusion porosimetry (MIP) in accordance with ASTM D4284-07 on a PoreMaster-60 (Quantachrome Corp.).

Table 1: Properties of slag.

Density (g/cm^3)	Specific surface area (m^2/kg)	LOI (%)
2.92	423	1.7

Fourier transform infrared (FTIR) spectra were collected using a Nicolet iS50 FTIR spectrometer in transmittance mode from wavenumbers 4000 to 400 cm^{-1} using a standard KBr technique.

Thermogravimetry and differential scanning calorimetry (TG-DSC) curves were obtained using a NETSZCH STA449C thermobalance with a heating ratio of 10°C/min in a nitrogen atmosphere.

X-ray diffraction (XRD) data were collected using a PANalytical X'Pert PRO diffractometer in a conventional Bragg–Brentano θ–2θ configuration. The CuKα X-ray ($\lambda = 1.5418$ Å) was generated using 40 mA and 40 kV. A Kβ nickel filter was used to remove the β diffraction spectra. The AAS samples were scanned continuously between 5° and 75° 2θ. The $d_{(002)}$ values were calculated by the Bragg equation [8]:

$$2\ d\ \sin\ \theta = n\lambda, \tag{1}$$

where d is the crystalline interplanar distance, θ is the grazing angle, n is the diffraction series, and λ is the X-ray wavelength.

The ^{29}Si MAS NMR spectra were recorded on a Bruker AVANCE III 500 spectrometer. The ^{29}Si chemical shift was referenced relative to tetramethylsilane, $Si(CH_3)_4$. The ^{29}Si MAS NMR spectra were deconvoluted using a Gaussian–Lorentzian function. The mean chain length of C-(A-)S-H (MCL) can be calculated by (2) [9]. The Al/Si ratio of C-(A-)S-H can be calculated by (3) [9]. The hydration degree of slag (α) of the slag can be calculated by (4) [10].

$$\mathrm{MCL} = \frac{2\left[Q^1 + Q^2 + (3/2)Q^2\,(1\mathrm{Al})\right]}{Q^1}, \tag{2}$$

$$\frac{\mathrm{Al}}{\mathrm{Si}} = \frac{(1/2)Q^2\,(1\mathrm{Al})}{Q^1 + Q^2 + Q^2\,(1\mathrm{Al})}, \tag{3}$$

$$\alpha = \left(1 - I_{\mathrm{slag}}^{\mathrm{rel}}\right) \times 100\%. \tag{4}$$

The chemical shifts are normally interpreted in terms of the different silicon $Q^n(m\mathrm{Al})$ environments, where n denotes the number of bridging oxygen linked to other $[SiO_4]$ tetrahedra (or $[AlO_4]^-$ tetrahedra) for each $[SiO_4]$ tetrahedral unit; m denotes the number of bridging oxygen linked to other $[AlO_4]^-$ tetrahedra for each $[SiO_4]$ tetrahedral unit. $I_{\mathrm{slag}}^{\mathrm{rel}}$ denotes the sum of relative integral intensity of Q^0 and Q_{slag}^1.

The specimens used for MIP, FTIR, XRD, TG-DSC, and ^{29}Si MAS NMR were vacuum-dried to a constant weight before being used.

3. Results and Discussion

3.1. Results

3.1.1. Autogenous Shrinkage. Figure 1 shows that the autogenous shrinkage of AAS mortar decreases with the increase of CaO content. The ordering of 252 d autogenous

Table 2: Main chemical content of slag (%).

CaO	SiO_2	Al_2O_3	MgO	SO_3	TiO_2	MnO	Fe_2O_3	Na_2O	K_2O
41.84	29.49	17.52	5.48	1.83	0.68	0.43	0.31	0.27	0.21

Table 3: Properties of fine aggregates.

Fineness modulus	Bulk density (kg/m^3)	Performance density (kg/m^3)	Particle size (mm)
2.5	1481	2590	<5

Table 4: Gradation of fine aggregate (residue on each sieve).

Mesh aperture	<0.15 mm	0.15 mm	0.30 mm	0.60 mm	1.18 mm	2.36 mm	4.75 mm
Residue on each sieve (%)	0.5	5.1	45.1	46	2.8	0.5	0.0

Table 5: Compositions of alkali-activated slag (AAS) cement.

Group	Activator	$m_{Na}:m_s$ (%)	$m_{Ca}:m_s$ (%)
C0	NaOH	4	0
C3		4	3
C6		4	6
C9		4	9
C12		4	12

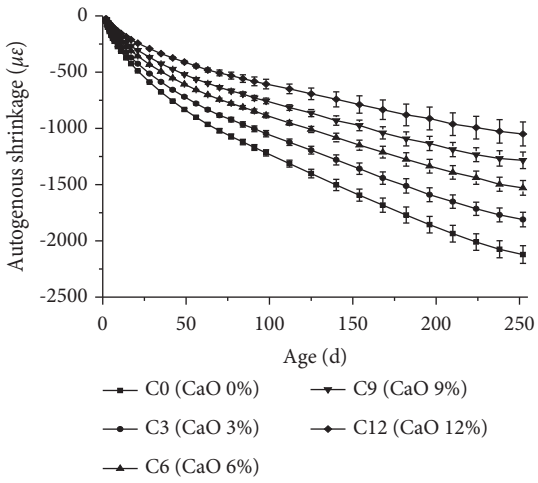

Figure 1: Autogenous shrinkage of AAS mortars.

shrinkage values of AAS mortars is C0 (2121.41 $\mu\varepsilon$) > C3 (1810.18 $\mu\varepsilon$) > C6 (1528.92 $\mu\varepsilon$) > C9 (1283.46 $\mu\varepsilon$) > C12 (1049.50 $\mu\varepsilon$).

3.1.2. Pore Structure. Pore size distributions of AAS pastes are shown in Figure 2 and Table 6. The total porosity and average pore diameter are shown in Table 6. The total porosities of C12 at 28 d and 56 d were 6.45% and 5.28% less than those of C0. The average pore diameters of C12 at 28 d and 56 d were 29.62% and 25.63% less than those of C0. These results indicate that the increase in CaO content results in the pore structure becoming finer in the AAS paste.

Figure 2 also shows that the threshold pore diameter of the first peak (around 7–9 nm) for C0 increases from 7.07 nm (28 d) to 8.24 nm (56 d). This indicates that some micropore closure occurs as hydration continues. However, the threshold pore diameter of the first peak (around 7–9 nm) for C12 increases slightly from 8.70 nm (28 d) to 8.73 nm (56 d).

3.1.3. FTIR. Figure 3 shows the FTIR spectra of the AAS pastes. The narrow bands at 3652–3641 cm^{-1} on the spectra are characteristic of the stretching vibrations generated by the O–H bonds in portlandite ($Ca(OH)_2$) [11]. It can be inferred that, due to the high initial Ca/Si ratio in C12, a certain amount of portlandite precipitated with the C-(A-)S-H gel. The bands at 3455–3524 cm^{-1} are the stretching vibrations of O–H, and the bands at 1652–1647 cm^{-1} are the bending vibrations of H–O–H [12].

Peaks typical of carbonate C–O bond asymmetric stretching vibrations are observed at 1456–1385 cm^{-1}. The bands at 897–896 cm^{-1} are the bending vibrations of $[CO_3]^{2-}$. These results show that some of the hydration products are carbonized.

The intense narrow bands at 954–949 cm^{-1} are typical of the Si–O asymmetric stretching vibrations generated by T–O–T (T: $[SiO_4]$ tetrahedra or $[AlO_3]^-$ tetrahedra). The band for C0 moves from 952 cm^{-1} (28 d) to 954 cm^{-1} (56 d). This indicates the increased polymerization of C-(A-)S-H [12]. The band for C12 also moves from 949 cm^{-1} (28 d) to 950 cm^{-1} (56 d). It indicates that the polymerization of C-(A-)S-H in C12 is less than that of C0, and the increased polymerization of C-(A-)S-H in C12 is less than that of C0 over 28–56 d. No Q^3 units were detected by this technique (i.e., at 1200 cm^{-1} [13]) during this study.

The bands at 669–664 cm^{-1} are attributed to the stretching vibrations of Al–O in $[AlO_3]^-$ tetrahedra. This result indicates that some of the Si in $[SiO_4]$ is substituted by Al. The band at 455–442 cm^{-1} is attributed to the bending vibrations of Si–O–Si and O–Si–O in C-(A-)S-H.

3.1.4. TG-DSC. Figure 4 shows the TG, DSC, and DTG curves of the hardened C0 and C12 pastes for 56 d curing. The presence of C-(A-)S-H in C0 and C12 is shown by the peaks below 200°C on the DSC and DTG curves. The weight loss on the TG curves in this temperature range are 8.37% (C0) and 7.41% (C12) and are related to C-(A-)S-H, Aft, and Afm [14].

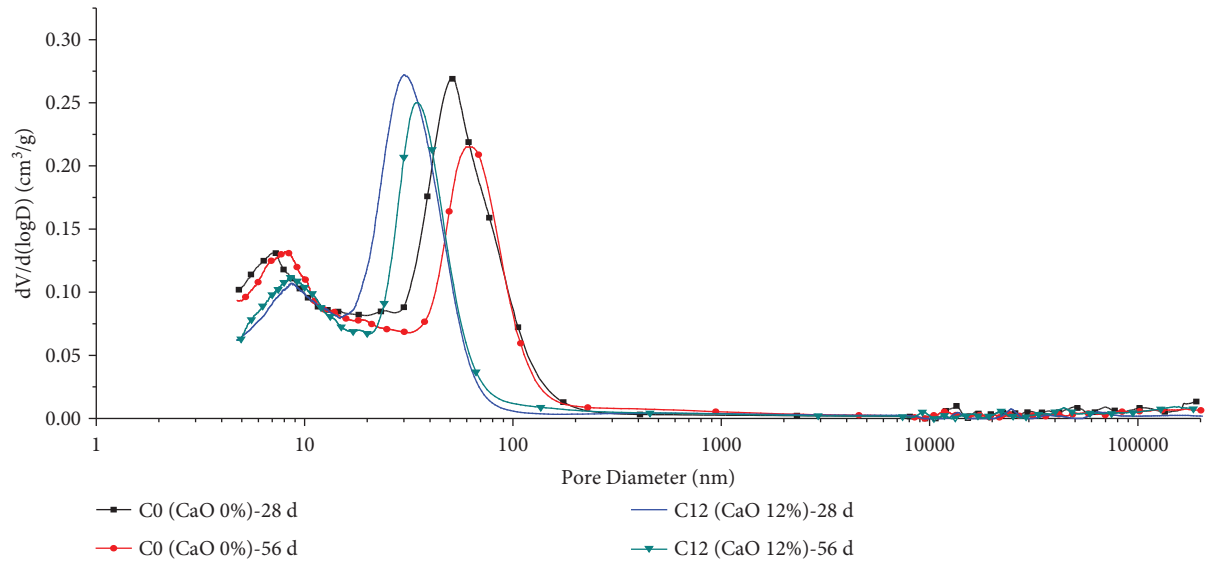

Figure 2: Pore size distribution of C0 and C12 at 28 d and 56 d.

Table 6: Total porosity, pore size distribution, and average pore diameter of C0 and C12 at 28 d and 56 d.

Group	Total porosity (%)	Average pore diameter (nm)	Pore size distribution (%)			
			<20 nm	20–50 nm	50–200 nm	>200 nm
C0-28 d	29.11	22.89	9.41	8.26	9.41	2.03
C0-56 d	27.80	20.51	10.03	6.79	8.96	2.02
C12-28 d	27.23	16.11	8.18	14.34	2.70	2.01
C12-56 d	26.33	15.25	9.07	12.67	2.59	2.00

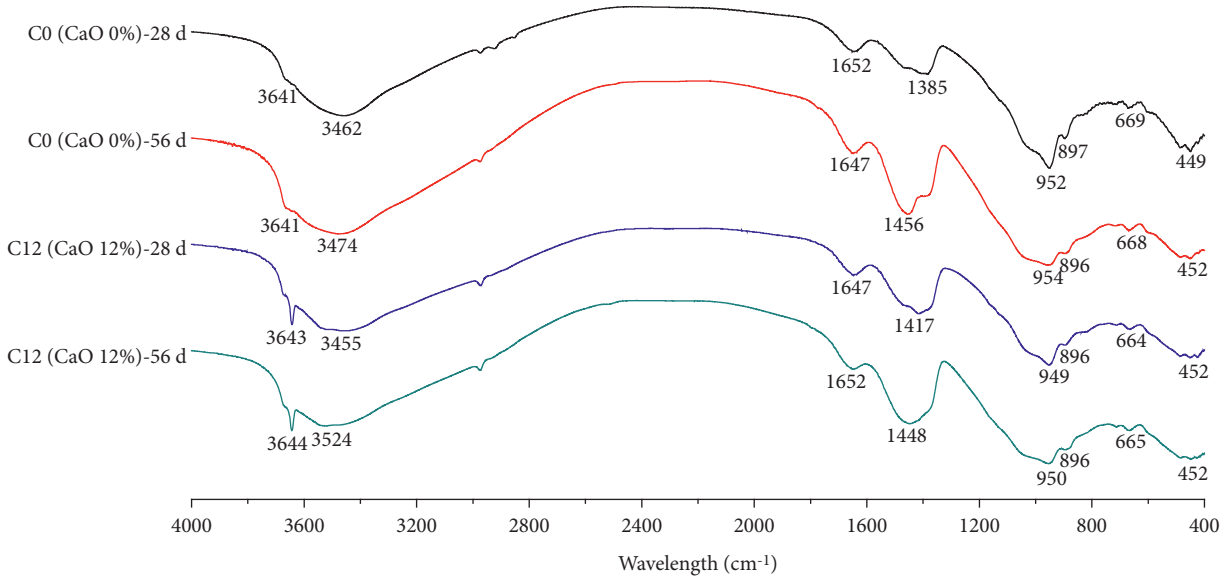

Figure 3: FTIR spectra of C0 and C12 at 28 d and 56 d.

The first hydrotalcite phase peak overlaps the C-(A-)S-H peak at 200–250°C, and the second broad peak occurs at 373.0°C (C0, Figure 4(a)) and 378.6°C (C12, Figure 4(b)) [15]. The weight losses for the second broad peak on the TG curve are 3.94% (C0, Figure 4(a)) and 3.38% (C12, Figure 4(b)). These results indicate a reduction of the hydrotalcite phase as CaO content increases.

The portlandite ($Ca(OH)_2$) peak occurs at 451.7°C on the DSC and DTG curves for C12 (Figure 4(b)), but there is no distinct peak in the temperature range 400°C–500°C on the DSC and DTG curves for C0 (Figure 4(a)). These results show that portlandite content increases with the increase of CaO content.

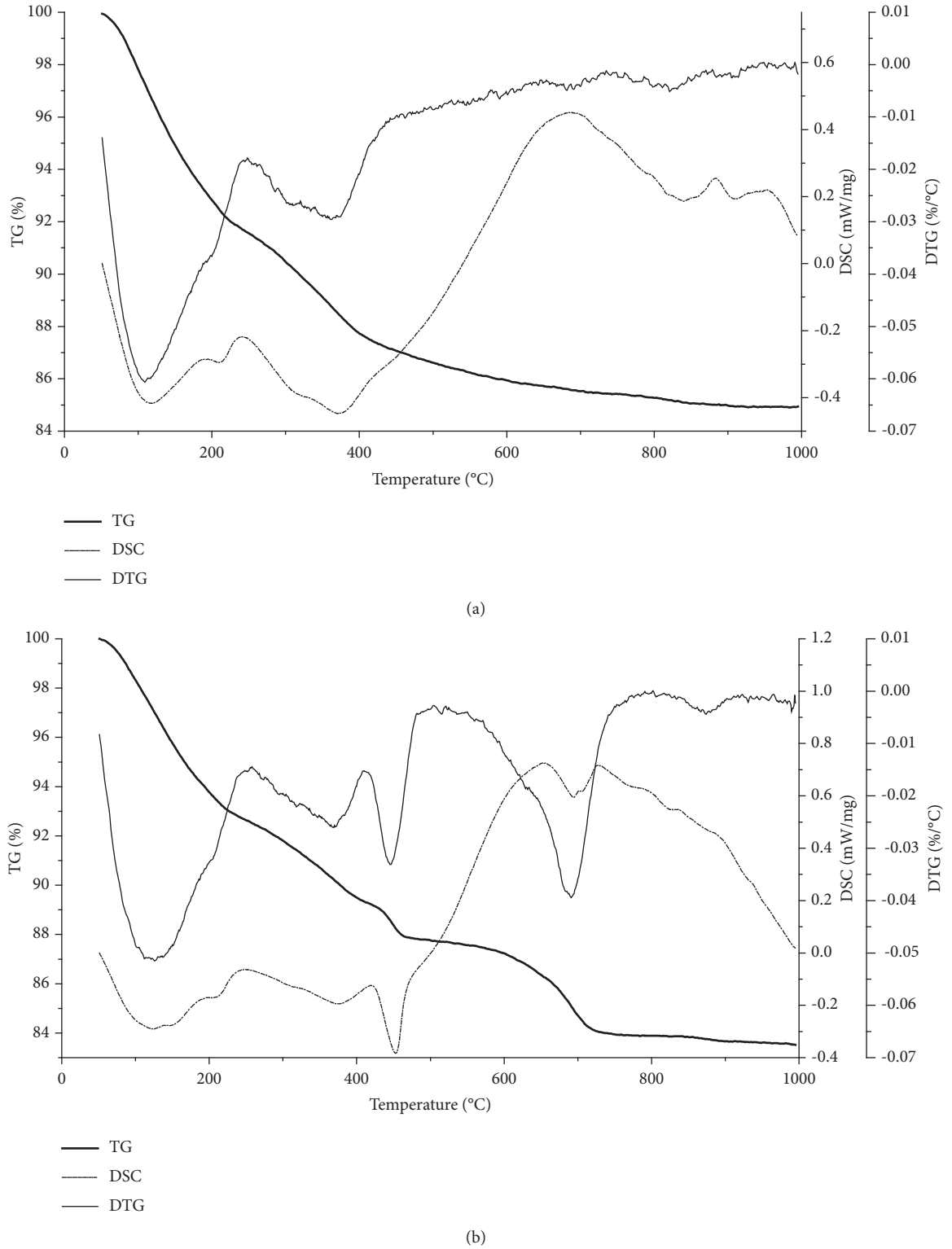

Figure 4: TG-DSC-DTG plots of C0 and C12 at 56d; (a) TG-DSC-DTG plots of C0 at 56d; (b) TG-DSC-DTG plots of C12 at 56d.

3.1.5. XRD. Figure 5 shows the XRD patterns of C0 and C12 at 28 d and 56 d. The hydration products in both C0 and C12 are C-S-H (I), hydrotalcite phases, hydrogarnet, ettringite, and portlandite, which is consistent with existing research [16]. Calcite was also detected in AAS due to slight carbonation during mixing or sample preparation. There is a considerable increase in peak intensity of portlandite and C-S-H (II) on the patterns for C12 at 28 d and 56 d. This

indicates an increase in portlandite content and the modification of the C-(A-)S-H nanostructure. The peak intensities corresponding to C-S-H (I), hydrogarnet and ettringite decreased and indicate that α decreases with the increase of CaO content.

Table 7 shows the mean basal distances ($d_{(002)}$) of C-S-H (I) in C0 and C12 at 28 d and 56 d. The $d_{(002)}$ values of C-S-H(I) in C0 and C12 at 56 d are 0.46% and 0.29% less than those at 28 d, respectively. It indicates that the mean basal distance of C-S-H (I) decreases with the age. The $d_{(002)}$ values of C-S-H(I) in C12 at 28 d and 56 d are 1.87% and 1.69% less than those in C0, respectively. It indicates that the mean basal distance of C-S-H (I) decreases with the addition of CaO. The percentage reduction of $d_{(002)}$ from 28 d to 56 d decreases with the addition of CaO.

3.1.6. ^{29}Si MAS NMR. Figure 6 shows the deconvolution of ^{29}Si MAS NMR patterns for C0 and C12 at 28 d and 56 d. The ranges of chemical shifts corresponding to Q^n and Q^n(1Al) units in aluminosilicate were used for fitting the NMR spectrum of AAS [17]. It can be seen that raw slag consists mainly of Q^0 and Q^1_{slag}, while C-(A-)S-H gel consists primarily of Q^1, Q^2(1Al), and Q^2. This indicates that there are no cross-link structures in the specimens. The signal corresponding to Q^2(1Al) indicates that some Si in the [SiO_4] was substituted by Al.

Table 8 shows the Al/Si ratio of C-(A-)S-H, MCL and α obtained by ^{29}Si MAS NMR. The MCLs in C12 at 28 d and 56 d are shorter than those in C0 at 28 d and 56 d. The MCLs in C0 and C12 at 56 d are longer than those in C0 and C12 at 28 d, respectively. The silicate chains of C-(A-)S-H consist of $3n-1$ [SiO_4] tetrahedra (or $[AlO_3]^-$ tetrahedra) [11]. The MCLs in C0 and C12 are in the range 5.20–6.04. Therefore, most of the silicate chains of C-(A-)S-H are pentamers. In addition, the Al/Si ratios of C-(A-)S-H in C12 at 28 d and 56 d are less than those in C0 at 28 d and 56 d.

The MCLs in C12 at 28 d and 56 d are 8.93% and 10.60% less than those in C0 at 28 d and 56 d, respectively. The MCL in C12 at 56 d is 3.85% greater than that at 28 d. The MCL in C0 at 56 d is 5.78% greater than that at 28 d. The percentage increase of MCL from 28 d to 56 d decrease with the addition of CaO. The α of C12 at 28 d and 56 d are 8.64% and 9.66% less than those of C0 at 28 d and 56 d, respectively.

3.2. Discussion

3.2.1. Pore Structure. Increased CaO content results in a finer pore structure in AAS paste (Figure 2 and Table 6). The threshold pore diameter of the first peak (around 7–9 nm) for C0 moves significantly from 28 d to 56 d (7.07 nm to 8.24 nm) (Figure 2). The threshold pore diameter of the first peak (around 7–9 nm) for C12 moves slightly from 28 d to 56 d (8.70 nm to 8.73 nm) (Figure 2). These results indicate that micropore closure, which is one cause of autogenous shrinkage, is reduced by the increased CaO content.

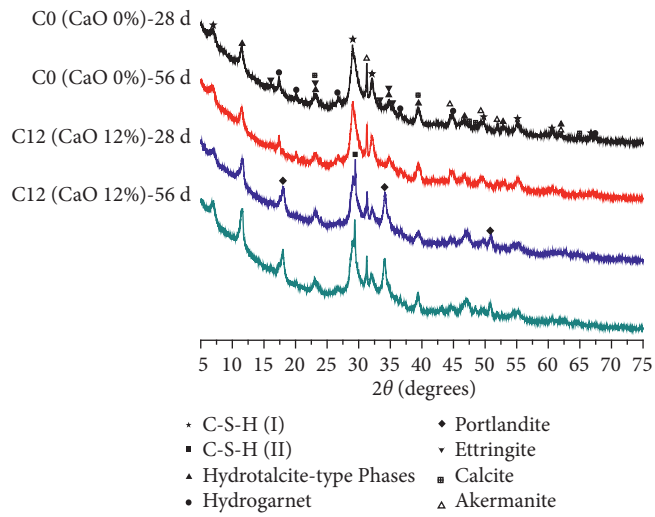

Figure 5: XRD patterns of C0 and C12 at 28 d and 56 d.

Table 7: Mean basal distances ($d_{(002)}$) of C-S-H(I) in C0 and C12 at 28 d and 56 d.

Group	Age (d)	2θ (°)	$d_{(002)}$ (Å)
C0	28	6.865	12.865
C0	56	6.897	12.806
C12	28	6.996	12.625
C12	56	7.016	12.589

3.2.2. Hydration Products and Hydration Degree. Analysis of the results of FTIR (Figure 3), TG-DSC-DTG (Figure 4), and XRD (Figure 5) shows that the amount of portlandite increases when the CaO content increases from 0% to 12%. The initial Ca/Si ratio of the AAS paste increases as CaO content increases. When the Ca/Si ratio of C-(A-)S-H is equilibrated with the pore solution, which is saturated with Ca^{2+}, the Ca^{2+} in the pore solution cannot be consumed to increase the Ca/Si ratio of C-(A-)S-H. Portlandite precipitates out and fills the capillary pores. The autogenous shrinkage of AAS is also counterbalanced by the volumetric expansion of calcium oxide's hydration.

The characteristic peak of C-S-H (II) is seen in the XRD spectrum for C12 (Figure 5). It is known that Ca/Si ratio of C-S-H (I) is 0.8–1.5, whereas the Ca/Si ratio of C-S-H (II) is approximately 1.8 in Portland cement [5]. This indicates that the Ca/Si ratio of C-(A-)S-H increases when the CaO content increases from 0 to 12% due to the increase in the initial Ca/Si ratio of the AAS paste. In addition, NaOH-activated slag (low Ca/Si ratio) was reported to be less stiff than OPC (high Ca/Si ratio) in the existing research [2].

Analysis of the results of TG-DSC-DTG (Figure 4), XRD (Figure 5), and ^{29}Si MAS NMR (Figure 6 and Table 8) shows that α at 28 d and 56 d decreases when the CaO content increases from 0 to 12%. In other words, the addition of CaO inhibits the hydration reaction. Thus the quantity of C-(A-)S-H, in which deformation mainly occurs, decreases as CaO content increases.

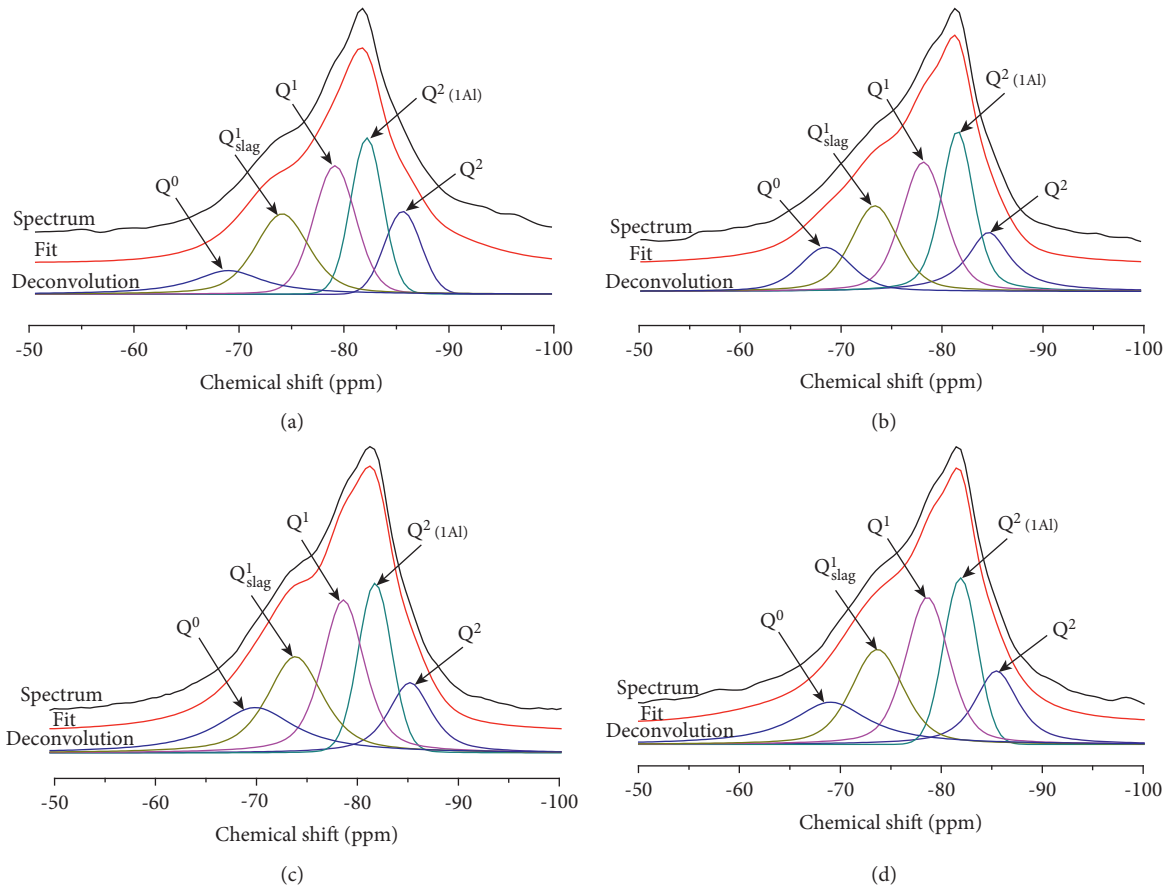

Figure 6: Deconvolution of ^{29}Si MAS NMR patterns: (a) C0-28d; (b) C0-56 d; (c) C12-28 d; (d) C12-56 d.

Table 8: Al/Si ratio of C-(A-)S-H, MCL and α obtained by ^{29}Si MAS NMR.

Group	Age (d)	Q^0 (%)	Q^1_{slag} (%)	Q^1 (%)	Q^2 (1Al) (%)	Q^2 (%)	MCL	Al/Si	α (%)
C0	28	11.60	23.84	26.77	23.71	14.07	5.71	0.18	64.55
C0	56	11.23	20.34	26.91	25.79	15.73	6.04	0.19	68.43
C12	28	18.07	22.96	26.40	19.41	13.16	5.20	0.16	58.97
C12	56	17.26	20.91	26.61	19.97	15.24	5.40	0.16	61.82

3.2.3. MCL and Mean Basal Distances of C-(A-)S-H. Analysis of the results of ^{29}Si MAS NMR (Figure 6 and Table 8) shows that Si polymerization occurs between adjacent C-(A-)S-H during hydration. The results of FTIR (Figure 3) agree with those of ^{29}Si MAS NMR. They indicate that MCL in AAS decreases as CaO content increases and that polymerization degree increases as curing time increases but it is inhibited by the addition of CaO. The addition of CaO initially increases the Ca/Si ratio of the AAS paste. This leads to an increase in the Ca/Si ratio of C-(A-)S-H. The MCLs decrease with the increase of Ca/Si ratio of C-(A-)S-H [11].

Deprotonation of ≡SiOH in C-(A-)S-H occurs in an alkaline environment as shown in

$$\equiv \mathrm{Si-OH} + \mathrm{OH^-}\ ] \equiv \mathrm{Si-O^-} + \mathrm{H_2O}. \quad (5)$$

Ca^{2+} and Na^+ in the solution compete to compensate the negative charge of $\equiv Si-O^-$. Ca^{2+} preferentially compensates the negative charge over Na^+ [18]. Thus adsorption of Na^+ decreases as Ca^{2+} concentration increases in the pore solution [19]. The increased polymerization of C-(A-)S-H during hydration (in (6)), which increases the density of C-(A-)S-H [20], is inhibited by the addition of CaO until the Ca/Si ratio of C-(A-)S-H reaches the maximum as it equilibrates with the Ca^{2+} saturated solution.

$$\equiv \mathrm{Si-ONa} + \mathrm{HO-Si} \equiv\ ] \equiv \mathrm{Si-O-Si} \equiv\ + \mathrm{NaOH}. \quad (6)$$

The Al/Si ratios of C-(A-)S-H in C12 are lower than those in C0 (Table 8). This indicates that the Al/Si ratios of C-(A-)S-H in AAS decrease when CaO is added. The reduction in MCL indicates a decrease in the proportion of bridge [SiO_4] tetrahedra (Q^{2b}). According to the result of the ab initio algorithm [21], Al is easier to substitute Si in Q^{2b} than that in Q^{2p}. Therefore, Al has a lower probability of substituting the Si of [SiO_4] tetrahedra in C-(A-)S-H when

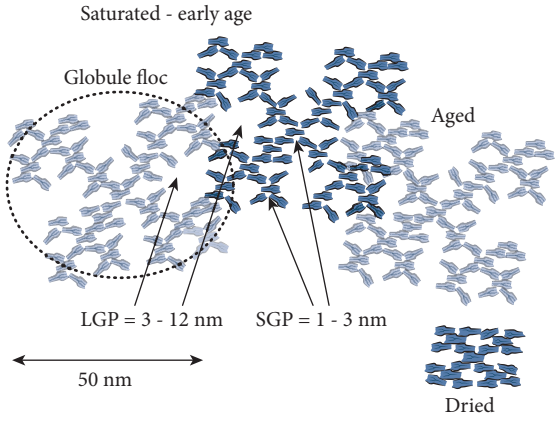

Figure 7: Rearrangement of C-(A-)S-H [22].

CaO is added. The substitution of Al^{3+} for Si^{4+} creates negative charge that is compensated by the uptake of Na^+ ions or Ca^{2+} ions in the gel [11]. Therefore, the amount of adsorbed Na^+ decreases as the Al/Si ratios of C-(A-)S-H decrease.

Analysis of the results of XRD (Table 7) shows that the mean basal distance of C-S-H (I) decreases with the age, which is caused by the rearrangement of C-S-H (I) (Figure 7) [22]. The percentage reduction of $d_{(002)}$ from 28 d to 56 d decreases with the addition of CaO. It indicates that the addition of CaO inhibits the rearrangement of C-S-H (I). The addition of CaO decreases the mean basal distance of C-S-H (I), which decreases the interlayer friction coefficients [23, 24], while the decrease in the quantity of adsorbed Na^+ increases the interlayer friction coefficients [23, 24]. The results show that this latter process is dominant. In addition, the adsorption of Na^+ results in a more irregular stacking of C-(A-)S-H [19] and then creates a larger space for shrinkage because of the differences in ionic radii.

4. Conclusions

This paper presents the effect of CaO on the autogenous shrinkage of alkali-activated slag (AAS) mortar, using NaOH ($Na_2O\% = 4\%$ by mass of slag) as an activator. Based on the experimental results, the following conclusions are drawn:

(1) C-S-H (I) (low stiffness) is partially replaced by C-S-H (II) (high stiffness) because of the addition of 12% CaO. In addition, the amount of portlandite increases as CaO content increases. These can lead to higher stiffness of AAS paste.

(2) The addition of CaO inhibits hydration. The hydration degrees of slag (α) in AAS with 12% CaO at 28 d and 56 d are 8.64% and 9.66% lower than those without CaO, respectively. In addition, the micropore closure, which is one cause of autogenous shrinkage, is inhibited by the addition of 12% CaO.

(3) The mean chain length of C-(A-)S-H (MCL) in AAS increases with curing age. The mean basal distances ($d_{(002)}$) of C-S-H(I) in AAS decrease with curing age. These can make the structure of C-(A-)S-H gel denser and lead to the autogenous shrinkage of AAS mortar. The increase of polymerization degree of C-(A-)S-H and rearrangement of C-S-H(I) during hydration are inhibited by the addition of CaO.

(4) The increase of polymerization degree of C-(A-)S-H and rearrangement of C-S-H(I) are also important composition of the autogenous shrinkage of AAS mortar besides the elastic deformation under the action of capillary force.

(5) The autogenous shrinkage of AAS mortar decreases with the increase of CaO content. The 252 d autogenous shrinkage of AAS mortar activated by NaOH ($Na_2O\% = 4\%$ by mass of slag) is reduced by 50.53% due to the addition of 12% CaO.

Data Availability

The data used to support the findings of this study are available from the corresponding author upon request.

Conflicts of Interest

The authors declare that there are no conflicts of interest regarding the publication of this paper.

Acknowledgments

This research was funded by National Natural Science Foundation of China (NSFC) (grant no. 51878179), Fujian Province Department of Education fund item (grant no. JAT190460), Natural Science Foundation of Fujian Province (grant no. 2020J01939), Science and Technology Planning Project of Fujian Province (grant no. 2019H6025), and Research and Innovation Team of Fujian Jiangxia University (grant no. 19KTXZ02).

References

[1] M. Jiang, X. Chen, F. Rajabipour, and C. T. Hendrickson, "Comparative life cycle assessment of conventional, glass powder, and alkali-activated slag concrete and mortar," *Journal of Infrastructure Systems*, vol. 20, no. 4, Article ID 04014020, 2014.

[2] C. Cartwright, F. Rajabipour, and A. Radlińska, "Shrinkage characteristics of alkali-activated slag cements," *Journal of Materials in Civil Engineering*, vol. 27, Article ID B4014007, 2015.

[3] A. Allahverdi, B. Shaverdi, and E. N. Kani, "Influence of sodium oxide on properties of fresh and hardened paste of alkali-activated blast-furnace slag," *Acta Medica Iranica*, vol. 49, pp. 304–314, 2010.

[4] A. A. M. Neto, M. A. Cincotto, and W. Repette, "Drying and autogenous shrinkage of pastes and mortars with activated slag cement," *Cement and Concrete Research*, vol. 38, no. 4, pp. 565–574, 2008.

[5] N. K. Lee, J. G. Jang, and H. K. Lee, "Shrinkage characteristics of alkali-activated fly ash/slag paste and mortar at early ages," *Cement and Concrete Composites*, vol. 53, pp. 239–248, 2014.

[6] A. A. M. Neto, M. A. Cincotto, and W. Repette, "Mechanical properties, drying and autogenous shrinkage of blast furnace

slag activated with hydrated lime and gypsum," *Cement and Concrete Composites*, vol. 32, no. 4, pp. 312–318, 2010.

[7] Astm International, *Astm c490/c490m-11. Standard Practice For Use Of Apparatus For The Determination Of Length Change Of Hardened Cement Paste, Mortar, And Concrete*, Astm International, West Conshohocken, PA, USA, 2014.

[8] S. Grangeon, F. Claret, Y. Linard, and C. Chiaberge, "X-ray diffraction: a powerful tool to probe and understand the structure of nanocrystalline calcium silicate hydrates," *Acta Crystallographica Section B Structural Science Crystal Engineering and Materials*, vol. 69, no. 5, pp. 465–473, 2013.

[9] I. G. Richardson and G. W. Groves, "The structure of the calcium silicate hydrate phases present in hardened pastes of white Portland cement/blast-furnace slag blends," *Journal of Materials Science*, vol. 32, pp. 4793–4802, 1997.

[10] G. Parry-Jones, A. J. Al-Tayyib, and A. I. Al-Mana, "Evaluation of degree of hydration in concrete using 29Si magic angle spinning NMR in solids," *Cement and Concrete Research*, vol. 18, no. 2, pp. 229–234, 1988.

[11] F. Puertas, M. Palacios, H. Manzano, J. S. Dolado, A. Rico, and J. Rodríguez, "A model for the C-A-S-H gel formed in alkali-activated slag cements," *Journal of the European Ceramic Society*, vol. 31, no. 12, pp. 2043–2056, 2011.

[12] W. Mozgawa and J. Deja, "Spectroscopic studies of alkaline activated slag geopolymers," *Journal of Molecular Structure*, vol. 924-926, pp. 434–441, 2009.

[13] I. García Lodeiro, D. E. Macphee, A. Palomo, and A. Fernández-Jiménez, "Effect of alkalis on fresh C-S-H gels. FTIR analysis," *Cement and Concrete Research*, vol. 39, no. 3, pp. 147–153, 2009.

[14] Y. Jeong, H. Park, Y. Jun, J. H. Jeong, and J. E. Oh, "Influence of slag characteristics on strength development and reaction products in a CaO-activated slag system," *Cement and Concrete Composites*, vol. 72, pp. 155–167, 2016.

[15] T. Hibino, "Decarbonation behavior of Mg-Al-CO3 hydrotalcite-like compounds during heat treatment," *Clays and Clay Minerals*, vol. 43, no. 4, pp. 427–432, 1995.

[16] M. Ben Haha, G. Le Saout, F. Winnefeld, and B. Lothenbach, "Influence of activator type on hydration kinetics, hydrate assemblage and microstructural development of alkali activated blast-furnace slags," *Cement and Concrete Research*, vol. 41, no. 3, pp. 301–310, 2011.

[17] B. Boddenberg, "High-resolution solid-state NMR of silicates and zeolites," *Applied Catalysis*, vol. 42, no. 1, pp. 187-188, 1988.

[18] C. Labbez, I. Pochard, B. Jönsson, and A. Nonat, "C-S-H/solution interface: experimental and Monte Carlo studies," *Cement and Concrete Research*, vol. 41, no. 2, pp. 161–168, 2011.

[19] B. Lothenbach and A. Nonat, "Calcium silicate hydrates: solid and liquid phase composition," *Cement and Concrete Research*, vol. 78, pp. 57–70, 2015.

[20] D. Ravikumar and N. Neithalath, "Effects of activator characteristics on the reaction product formation in slag binders activated using alkali silicate powder and NaOH," *Cement and Concrete Composites*, vol. 34, no. 7, pp. 809–818, 2012.

[21] L. Pegado, C. Labbez, and S. V. Churakov, "Mechanism of aluminium incorporation into C-S-H from ab initio calculations," *Journal of Materials Chemistry*, vol. 2, no. 10, pp. 3477–3483, 2014.

[22] H. M. Jennings, "Refinements to colloid model of C-S-H in cement: cm-II," *Cement and Concrete Research*, vol. 38, no. 3, pp. 275–289, 2008.

[23] L. Ma, A. Gaisinskaya-Kipnis, N. Kampf, and J. Klein, "Origins of hydration lubrication," *Nature Communications*, vol. 6, no. 1, p. 6060, 2015.

[24] A. Gaisinskaya-Kipnis, L. Ma, N. Kampf, and J. Klein, "Frictional dissipation pathways mediated by hydrated alkali metal ions," *Langmuir*, vol. 32, no. 19, pp. 4755–4764, 2016.